

A Journal of the Gesellschaft Deutscher Chemiker

Angewandte Chemie

GDCh

International Edition

www.angewandte.org

Accepted Article

Title: Piezo-Photocatalytic Synergy in BiFeO₃@COF Z-Scheme Heterostructures for High-Efficiency Overall Water Splitting

Authors: Mei-Ling Xu, Meng Lu, Guan-Ying Qin, Xiu-Mei Wu, Ting Yu, Li-Na Zhang, Kui Li, Xin Cheng, and Ya-Qian Lan

This manuscript has been accepted after peer review and appears as an Accepted Article online prior to editing, proofing, and formal publication of the final Version of Record (VoR). The VoR will be published online in Early View as soon as possible and may be different to this Accepted Article as a result of editing. Readers should obtain the VoR from the journal website shown below when it is published to ensure accuracy of information. The authors are responsible for the content of this Accepted Article.

To be cited as: *Angew. Chem. Int. Ed.* **2022**, e202210700

Link to VoR: <https://doi.org/10.1002/anie.202210700>

RESEARCH ARTICLE

Piezo-Photocatalytic Synergy in BiFeO₃@COF Z-Scheme Heterostructures for High-Efficiency Overall Water SplittingMei-Ling Xu[†], Meng Lu[†], Guan-Ying Qin, Xiu-Mei Wu, Ting Yu, Li-Na Zhang, Kui Li^{*}, Xin Cheng^{*}, and Ya-Qian Lan^{*}

Abstract: Solar-driven overall water splitting is an ideal way to generate renewable energy while still challenging. For the first time, this work combined covalent organic frameworks (COFs) and piezoelectric material by covalent linkages to form Z-scheme core@shell heterostructure for overall water splitting. Benefiting from the synergistic effect between the polarized electric field and photo-generated charges, as well as the precise adjustment of shell thickness, the carrier separation and utilization efficiency is greatly improved. The optimal BiFeO₃@TpPa-1-COF photocatalyst revealed hydrogen (H₂) and oxygen (O₂) production rates of 1416.4 and 708.2 μmol·h⁻¹·g⁻¹ under the excitation of ultrasonication coupled with light irradiation, which is the best performance among various piezo- and COF-based photocatalysts. This provides a new sight for the practical application of highly efficient photocatalytic overall water splitting.

Introduction

Hydrogen energy, as an important part of the future worldwide energy system, has the advantages of high calorific value, clean and abundant reserves^[1]. Photocatalytic overall water splitting to H₂ and O₂, which does not rely on cost-increasing and polluting sacrificial agents, is considered the most efficient and green way to utilize renewable energy^[2]. Researchers are committed to improving the catalytic efficiency of overall water splitting by constructing heterostructures, ion doping, as well as regulating the size and morphology for semiconductors^[3]. Nevertheless, the currently studied photocatalysts for overall water splitting are mainly based on oxides with low solar energy utilization efficiency^[4], their practical application is restricted by the confined separation and migration efficiency of photo-generated charges, and insufficient kinetic overpotentials for redox^[5]. Therefore, designing new narrow-gap and earth-abundant material systems and exploring effective methods to enhance the separation

efficiency of carriers and reaction thermodynamics is crucial for the industrial application of overall water splitting.

Covalent organic frameworks (COFs), as an emerging class of porous organic material with ordered crystal structure, are composed of lightweight elements and connected by covalent bonds^[6]. Recently, COFs have been applied in various fields, including photocatalysis, gas adsorption and storage and ionic conduction^[7]. Among them, TpPa-1-COF has been recognized as an outstanding metal-free photocatalyst for water splitting owing to high surface area, adjustable topologies structure and simple chemical modification^[8]. In particular, the TpPa-1-COF represent extensive optical absorption, excellent thermal and chemical stability, which is attributed to the absorption of characteristic groups and large conjugated systems^[9]. To date, researchers have been tried to construct reasonable COFs/inorganic semiconductor hybrid or even Z-scheme heterostructures to promote the separation and transfer of photo-generated charges, such as TpPa-1-COF-MoS₂^[10], TpPa-1-COF-TiO₂^[9b] and TpPa-2-COF/α-Fe₂O₃^[11]. However, the current COFs and their heterojunctions still cannot effectively drive the overall water splitting reaction due to the lack of sufficient oxidation potential for holes and efficient separation, transport and utilization of carriers^[8b, 12]. Thence, it is urgent and necessary to introduce a stronger driving force to further improve the photocatalytic overall water splitting.

Fortunately, the introduction of external or built-in fields has been proven to be an effective way to accelerate the separation and transfer of photo-generated charge carriers through piezoelectric potential as a continuous driving force^[13], which can induce various catalytic reactions, including water splitting, organic pollutant degradation and sterilization^[14]. Numerous piezoelectric/ferroelectric nanomaterials, such as ZnO^[15], BiFeO₃^[16], BaTiO₃^[17], KNbO₃^[18], and lead zirconate titanate (PZT)^[19] have been exploited in the area of photocatalysis. A popular strategy is to construct heterojunctions by coupling semiconductor photocatalysts and piezoelectric materials to achieve the intelligent integration of semiconductor photoelectric properties and piezoelectric effects. In detail, the piezoelectric polarization charge from the piezoelectric will provoke band bending at the interface, thereby attracting photo-generated carriers with opposite charges^[20]. A series of coupling materials have improved the separation of photo-generated carriers via the polarization electric field excited by periodic ultrasonic waves for the decomposition of organic pollutants, such as Ag₂O/BaTiO₃^[21], BiFeO₃/TiO₂^[16b], and ZnO/BaTiO₃^[22]. Whereas, few piezo-photo heterostructure materials mediate the overall water splitting reaction due to their low light absorption efficiency, insufficient catalytic active sites, single structure and weak interactions interaction in the heterostructure^[23]. Consequently, the development of piezoelectric-based heterojunctions with narrow band gaps, tunable structures and high-efficient for overall water

[*] Dr. M-L Xu,^[†] Mr. G-Y Qin, Miss. X-M Wu, Miss. T Yu, Prof. K. Li^{*} School of Materials Science and Engineering, University of Jinan, Jinan 250022, P. R. China.
E-mail: mse_lik@ujn.edu.cn
Dr. M-L Xu,^[†] Prof. L-N. Zhang, Prof. X. Cheng^{*} Shandong Provincial Key Laboratory of Preparation and Measurement of Building Materials, University of Jinan, Jinan, 250022, P. R. China.
E-mail: chengxin@ujn.edu.cn
Dr. M Lu,^[†] Prof. Y-Q Lan^{*} School of Chemistry, South China Normal University, Guangzhou 510006, P. R. China.
E-mail: yqlan@m.scnu.edu.cn; yqlan@njnu.edu.cn

[†] These authors contributed equally to this work.

Supporting information for this article is available on the WWW under <http://www.angewandte.org> or from the author.

RESEARCH ARTICLE

splitting has important theoretical significance and practical application.

Herein, for the first time, we combined COF and piezoelectric material by covalent bonds to form a high-efficient Z-scheme heterostructure piezo-photocatalyst for overall water splitting. An excellent visible-light harvesting TpPa-1-COF obtained by Schiff base reaction was controllably grown on amino-functionalized BiFeO₃ nanosheets to construct BiFeO₃@TpPa-1-COF core-shell hybrid material. Benefiting from the synergistic effect between the separation of carriers by the polarization potential generated built-in electric field in the BiFeO₃ nanosheets and abundant active sites of TpPa-1-COF, the transportation and application efficiency of carriers are greatly improved. Among them, TpPa-1-COF favors trapping of electrons, while BiFeO₃ tends to collect holes. In particular, BiFeO₃@TpPa-1-COF (BFO@COF20-C) exhibits unprecedented H₂ and O₂ production rates of 1416.4 and 708.2 μmol·h⁻¹·g⁻¹.

Results and Discussion

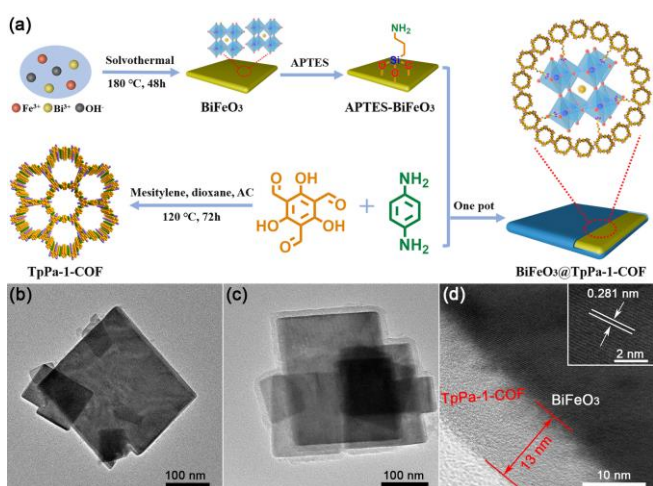


Figure 1. (a) Schematic illustration of the synthesis of the BiFeO₃@TpPa-1-COF heterostructure with covalently linked. TEM images of (b) BiFeO₃, (c) BFO@COF20-C, (d) High-resolution TEM image of BFO@COF20-C.

The schematic illustration depicting the synthesis of the BiFeO₃@TpPa-1-COF Z-scheme heterostructure is shown in **Figure 1a**. BiFeO₃ nanosheets were synthesized according to the reported solvothermal method with Bi(NO₃)₃·5H₂O and FeCl₃·6H₂O as precursor. Subsequently, 3-aminopropyltriethoxysilane (APTES) was selected to modify and get amino functionalized BiFeO₃ (APTES-BiFeO₃). The final covalently bonded BiFeO₃@TpPa-1-COF core-shell heterostructure with different mass ratios was synthesized by adding APTES-BiFeO₃ into the synthetic reaction system of TpPa-1-COF. The morphological peculiarities of the BiFeO₃, TpPa-1-COF and BiFeO₃@TpPa-1-COF heterostructure were studied through scanning electron microscopy (SEM) and transmission electron microscopy (TEM). As shown in **Figure S1**, the as-prepared TpPa-1-COF is a cluster-like morphology assembled from nanowires. The as-synthesized BiFeO₃ presented a square nanosheet structure with a smooth surface

and the length in the range of 100-300 nm (**Figure S2a and 1b**). It can clearly find that BiFeO₃ nanosheets are roughened and evenly covered with a shell layer from the SEM image of BiFeO₃@TpPa-1-COF (**Figure S2b-d**). The outcomes of TEM, high-resolution transmission electron microscopy (HR-TEM) and correlated elemental mapping images further substantiated that the BiFeO₃ nanosheets were encapsulated by TpPa-1-COF, forming a core-shell heterojunction with a covering thickness of 8-24 nm (**Figure 1c and S2e-g**). The interplanar spacing of 0.281 nm corresponds to the lattice fringes of (110) plane of the BiFeO₃ (**Figure 1d**).

The crystal structure and crystallinity of the as-synthesized samples were analyzed via Powder X-ray diffraction (PXRD). A series of BiFeO₃@TpPa-1-COF heterojunctions can observe the characteristic diffraction peaks of both BiFeO₃ and TpPa-1-COF, indicating the successful synthesis of heterojunctions (**Figure S3**). Additionally, the coexistence bands of BiFeO₃ and TpPa-1-COF in the Fourier transform infrared (FT-IR) spectrum of BiFeO₃@TpPa-1-COF further proves the successful preparation of heterojunction materials (**Figure S4**)^[11] ^[24]. Besides, the FT-IR spectroscopy of samples certificate the successful modification of BiFeO₃ (APTES-BiFeO₃) and the covalent connection between BiFeO₃ and TpPa-1-COF in BiFeO₃@TpPa-1-COF heterojunction (**Figure S5**)^[25], which indicates TpPa-1-COF has been successfully grafted on the surface of BiFeO₃ by Schiff base reaction^[26]. To further confirm that the two components in the BiFeO₃@TpPa-1-COF heterostructures were covalently linked, UV-vis diffuse reflectance spectra (DRS) examination was performed to investigate their reflection edges. As shown in **Figure S6**, the DRS spectrum of BFO@COF20-C demonstrates effective expansion absorption with only one reflection edge, which is similar to maternal TpPa-1-COF. The BFO-COF20 without covalent bond between the two components as comparison sample exhibits two apparent reflection edges from BiFeO₃ and TpPa-1-COF individually. This indicates the formation of a new hybrid material from in situ reaction.

In order to reveal the composition and valence of the TpPa-1-COF and BFO@COF20-C, X-ray photoelectron spectroscopy (XPS) characterization was carried out (**Figure S7**). The results show that the interface of BiFeO₃ and TpPa-1-COF exists strong interaction. Moreover, the thermogravimetric analysis (TGA) under argon atmosphere declares that TpPa-1-COF and BiFeO₃@TpPa-1-COF maintain excellent stability up to 400 °C (**Figure S8**). Meanwhile, the N₂ adsorption and desorption isotherms of as-synthesized samples were implemented at 77 K and all curves conform to the reversible type I isotherms according to the IUPAC classification (**Figure S9**). Pure BiFeO₃ nanosheets display the lowest Brunauer-Emmett-Teller (BET) surface area of 39 m²g⁻¹. As expected, the BET surface area of BiFeO₃@TpPa-1-COF (258 m²g⁻¹) is significantly lower than TpPa-1-COF (314 m²g⁻¹) due to the introduction of BiFeO₃. The optical absorption capacity and electronic band structure of the samples were evaluated by DRS and Mott-Schottky (M-S) spectra. As shown in **Figure S10**, all samples have a strong visible-range absorption, and the optical absorption edge is at around 650 nm. With the increase of BiFeO₃ content, the absorbance intensity of the BiFeO₃@TpPa-1-COF heterojunction enhanced. The corresponding band gaps of TpPa-1-COF and BiFeO₃ are calculated as 2.13 and 2.26 according to Kubelka-Munk, respectively (**Figure S11**). Furthermore, combining the M-S

RESEARCH ARTICLE

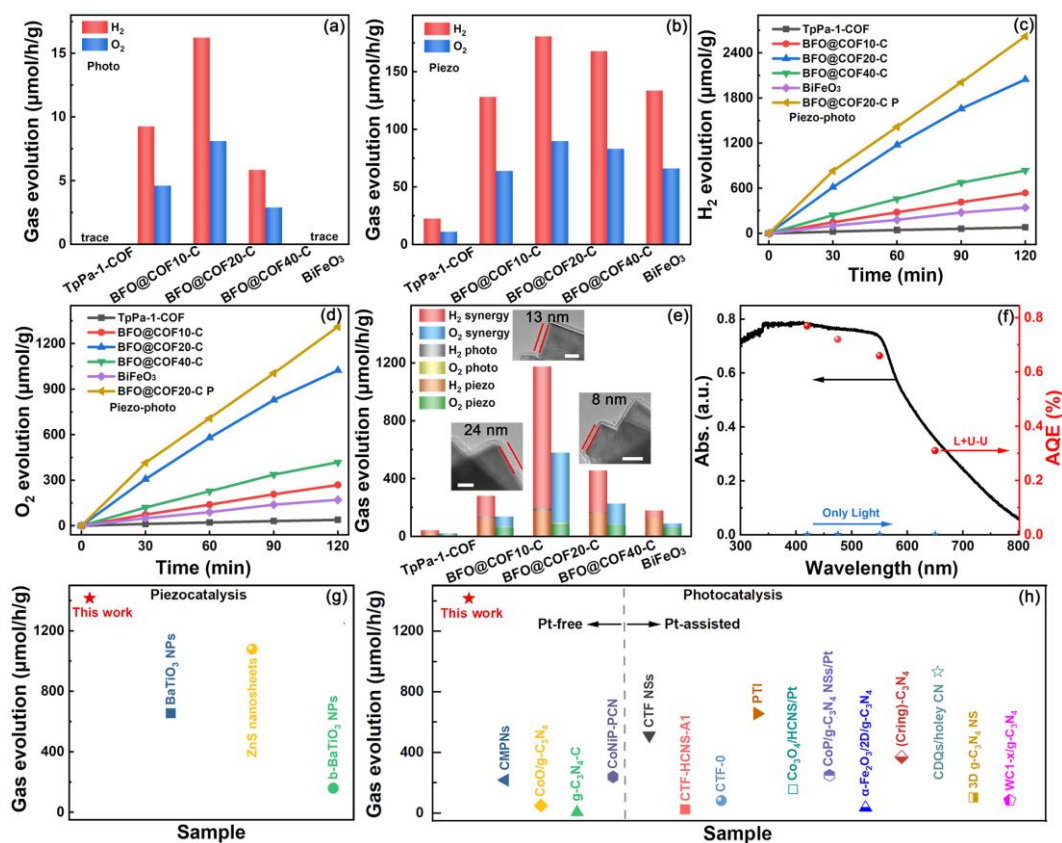


Figure 2. Rate of H₂ and O₂ production of (a) photocatalysis, (b) piezocatalysis, (c-d) piezo-photocatalysis and (e) synergy effect for samples. The insets show TEM images of BFO@COF10-C, BFO@COF20-C and BFO@COF40-C with the scale of 50 nm. (f) Wavelength-dependent apparent quantum efficiencies (AQE) of BFO@COF20-C. Comparison of catalytic overall water splitting rate of BFO@COF20-C over (g) COF and C₃N₄-based photocatalysts, (h) piezocatalysts.

results of TpPa-1-COF and BiFeO₃ confirms that the BiFeO₃@TpPa-1-COF heterojunction shows the Z-scheme system (Figure S12-13).

In order to verify the effect of polarization electric field in BiFeO₃@TpPa-1-COF on carrier separation, the photocatalytic, piezocatalytic, and piezo-photocatalytic overall water splitting were performed under light illumination, ultrasonic vibration and light with ultrasound coirradiation, respectively. Under visible light irradiation (Figure 2a), BiFeO₃ nanosheets cannot achieve photocatalytic overall water splitting owing to the conduction band (CB) with unfavorable for the hydrogen evolution reaction. TpPa-1-COF shows negligible photocatalytic H₂ and O₂ precipitation rates, which may be attributed to the rapid recombination of electron-hole pairs. Notably, the photocatalytic activity of the BiFeO₃@TpPa-1-COF heterostructures is evidently increased. Among them, BFO@COF40-C presented reduced photocatalytic activity. The reason for the phenomenon could be the shielding effect and unnecessary recombination caused by excessive BiFeO₃ nanosheets. The control measurement without light irradiation was also performed, confirming the hydrogen was generated by photocatalytic reaction (Figure S14). In addition, via only ultrasonic vibration (Figure 2b), BiFeO₃ nanosheets have higher piezo-catalytic performance due to outstanding piezoelectricity (133.7 μmol h⁻¹g⁻¹ and 66.2 μmol h⁻¹g⁻¹). It is worth noting that the piezoelectric catalytic activity of the

BiFeO₃@TpPa-1-COF heterostructures (180.7 μmol h⁻¹g⁻¹ and 89.9 μmol h⁻¹g⁻¹) with a large number of free carriers are further enhanced compared with pure TpPa-1-COF and BiFeO₃ nanosheets. Although it is proved that the combination of TpPa-1-COF and BiFeO₃ is beneficial to the improvement of the piezocatalytic reaction activity, the modification is limited because of the recombination of carriers at the two-phase interface. Excitingly, the piezo-photocatalytic activity of all samples is much higher than that of alone photocatalysis or piezoelectric catalysis under the synergistic effect of visible light irradiation and ultrasonic vibration in Figure 2c-d. Since piezoelectric properties can be significantly improved by electric poling, we tried to pole the as-prepared BFO@COF20-C nanoparticles^[27]. The results indicate that the H₂ and O₂ production rates of BFO@COF20-C are further improved to 1416.4 μmol h⁻¹g⁻¹ and 708.2 μmol h⁻¹g⁻¹, respectively. This significant enhancement can be allocated to the fact that the polarized electric field in TpPa-1-COF and BiFeO₃ nanosheets can effectively promote the separation and transfer of electron-hole pairs, resulting in more carriers participating in the redox catalytic reaction. To better understand the synergy effect of piezocatalytic and photocatalysis, the piezo-photocatalytic synergistic activity is determined as the amount of hydrogen or oxygen released by piezo-photocatalysis minus the sum of the piezocatalytic and photocatalytic evolution of hydrogen or oxygen. As presented in Figure 2e, the piezo-photo synergy effect of

RESEARCH ARTICLE

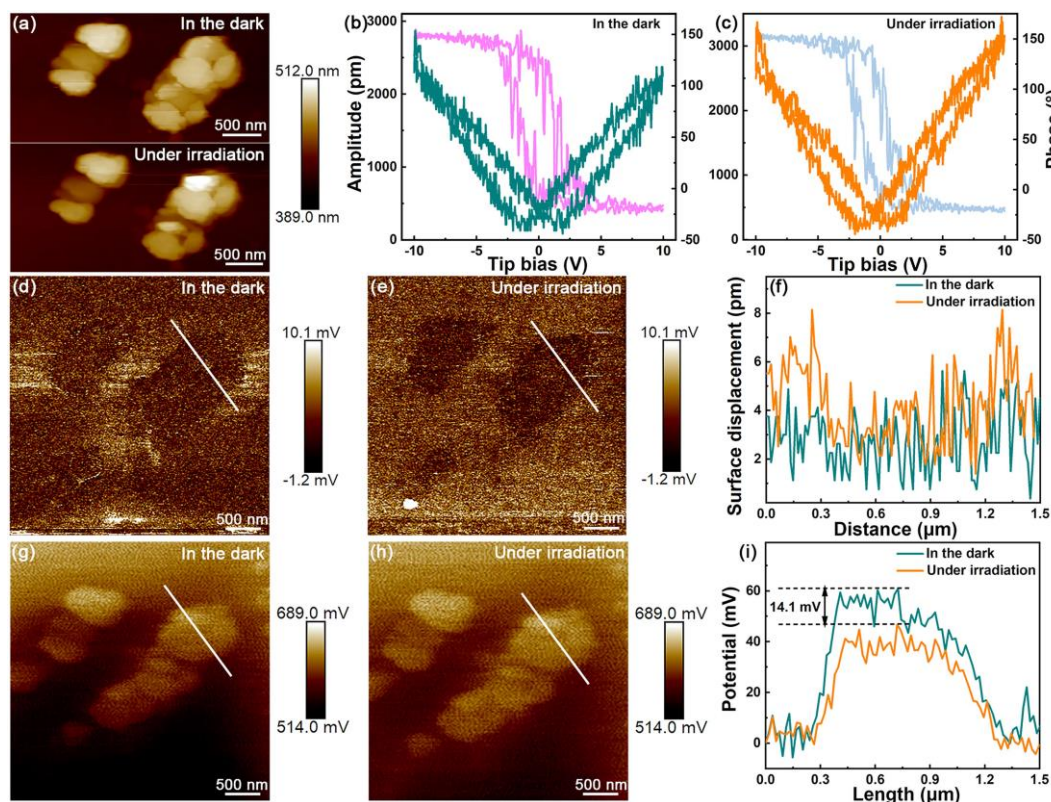


Figure 3. (a) The topographic images, displacement-voltage curve and phase curve (b) in the dark and (c) under illumination, amplitude images (d) in the dark and (e) under illumination, (f) surface height PFM image, KPFM potential images (g) in the dark and (h) under illumination, (i) surface potential curves of BiFeO₃@TpPa-1-COF.

BFO@COF20-C is significantly enhanced, indicating that the polarization electric field plays an important role in promoting the piezo-photocatalytic activity. However, the reduced catalytic activity of BFO@COF10-C may be due to the thick TpPa-1-COF shell covering the BiFeO₃ core, resulting in a stronger potential barrier between water molecules and photo-generated charges and weak light absorption. The carrier transport rate of BFO@COF40-C is slow owing to the small number of TpPa-1-COF generated on BiFeO₃ nanosheets. Interestingly, the piezo-photocatalytic activity of BFO@COF20-C is approximately 3.4 times higher than that of BFO-COF20 (Figure S15), which illustrates that the covalent bonds connection between two components play an important role in boosting the overall water splitting. Simultaneously, the BFO@COF20-C heterostructure demonstrated the outstanding apparent quantum efficiencies (AQE) value of 0.77% at 420 nm (Figure 2f and Table S1-2), which is significantly higher than the AQE under light irradiation only because the presence of the built-in electric field can effectively promote carrier transport and separation. The structural and morphology integrity of BFO@COF20-C in the piezo-photocatalytic reaction were confirmed by PXRD, FT-IR and TEM measurements of the sample after the reaction (Figure S16-18). Furthermore, we have made a comprehensive comparison of the previously reported overall water splitting performance of piezoelectric^[28], COF and C₃N₄ materials^[29], the results indicate that the catalytic activity of BFO@COF20-C is among the best (Figure 2g-h and Table S3), which further shows

that the combination of BiFeO₃ and TpPa-1-COF is beneficial to improve the activity of the piezo-photocatalytic reaction.

Generally, the application of external stress on the surface of the piezoelectric material can cause the charge centers of the cations and anions to be asymmetric, generate an internal electric field, thereby driving the separation of photo-generated carriers^[30]. In order to investigate piezoelectric properties of BiFeO₃ and BiFeO₃@TpPa-1-COF, the atomic force microscopy (AFM) with piezoresponse force microscope (PFM) was carried out. The surface structure of BiFeO₃ and BiFeO₃@TpPa-1-COF can be clearly observed in the topographic images (Figure S19a and Figure 3a), which is in accord with SEM and TEM images investigation. When a voltage of ± 10 V is applied to the surface of the samples, the emblematic butterfly-shaped amplitude loops and phase curves demonstrate typical piezoelectric properties of BiFeO₃ and BiFeO₃@TpPa-1-COF (Figure S19b-c and Figure 3b). Moreover, the maximum effective piezoelectric coefficient d_{33} can be quantitatively calculated through the slope of the amplitude loop, where the approximate d_{33} values of BiFeO₃ and BiFeO₃@TpPa-1-COF are ≈ 245 and 279 pm V⁻¹, respectively. It is worth noting that BiFeO₃@TpPa-1-COF displays very little H₂ and O₂ yield under illumination, but has the highest H₂ and O₂ yield in the piezo-photocatalytic process. For insights to the piezo-photo synergy enhanced catalytic process, a series of vertical PFM with amplitude scans and locally piezoelectric signals, and Kelvin probe force microscopy (KPFM) with the surface potential of BiFeO₃@TpPa-1-COF were measured under dark and

RESEARCH ARTICLE

illumination conditions. The amplitude loop moves significantly to the negative bias under illumination (**Figure 3c**), resulting in an asymmetric behavior with the right part of the loop stretched in the direction of the positive bias. This means that light has a positive effect of application, bringing about a greater piezoelectric response ($d_{33} \approx 291 \text{ pm V}^{-1}$) at zero bias. Furthermore, the vertical PFM amplitude scans area under illumination emerge brighter than in the dark, revealing the larger piezoresponse signals (**Figure 3d-e**). In order to more detailed analysis, **Figure 3f** shows the cross-sectional profile of the transition from the piezoresponse signal to the surface displacement along the white line. Interestingly, the scan under illumination exhibits a noticeably upward shift compared to the original value in the dark, indicating that the piezoresponse signals of the entire domain and the domain wall are enhanced. The strengthened piezoelectricity of $\text{BiFeO}_3@ \text{TpPa-1-COF}$ can generate more polarized charges under irradiation, thereby effectively promoting surface redox reactions. Besides, the surface potential of $\text{BiFeO}_3@ \text{TpPa-1-COF}$ is recorded in the dark and under irradiation by KPFM. As manifested in **Figure 3g-i**, it can be revealed a surface potential of 61.3 mV in the dark, which reduces to 47.2 mV after light irradiation. These results can be attributed to the existence of the built-in electric field and the dipoles formed by the charge transfer in $\text{BiFeO}_3@ \text{TpPa-1-COF}$ ^[31], contributing to the piezo-induced polarization charge partially depleted by photo-generated carriers,

which is beneficial to the separation of photo-generated charges and the improvement of catalytic activity.

In order to further reveal the promotion of the piezoelectric effect on the reaction thermodynamics, the Gibbs free energy change (ΔG) of the intermediate states involved in the oxygen evolution reaction (OER) and hydrogen evolution reaction (HER) reactions is calculated by density functional theory (DFT). The results of the following calculations are carried out under the condition of pH=7. The photocatalytic water oxidation belongs to a four-electron transfer process releasing one proton and one electron at each step (see computational details in Supporting Information)^[32]. **Figure 4a and S20-21** shows the possible intermediate (*OH, *O, and *OOH) atomic configurations along with the reaction route for oxygen evolution reaction (OER) process. Simultaneously, the hydrogen evolution reaction (HER) may involve two single electron transfer processes driven by photo-generated electrons, corresponding to the formation of *H intermediates on the surface of the photocatalyst (**Figure 4b and S22-23**). To gain an in-depth understanding of the intrinsic mechanism of piezo-photocatalytic activity, the ΔG of hydrogen and oxygen adsorption on different sites of $\text{BiFeO}_3@ \text{TpPa-1-COF}$ were investigated individually (**Figure S24-25**). The Gibbs free energy change of intermediate states clearly elucidated that the O site in TpPa-1-COF acts as the optimal catalytic active center for *H coordination, while the Fe site in BiFeO_3 acts as the optimal catalytic active center for the OER reaction process (**Figure S26-27 and Table S4-7**). The Gibbs free energy change curves in the four steps of the OER process are illustrated in **Figure 4c-d**. When no additional potential is applied, that is, without irradiation ($U=0 \text{ eV}$), the four reaction steps involved in all samples are endothermic, and the formation of *OOH is the endergonic rate-limiting step with highest ΔG ($\Delta G_{\text{highest}}$). Compared with TpPa-1-COF (2.09 eV) and BiFeO_3 (1.95 eV), $\text{BiFeO}_3@ \text{TpPa-1-COF}$ (1.63 eV) has the lowest $\Delta G_{\text{highest}}$, implying that the construction of heterostructures is more favorable for OER reaction. Further introducing a polarization electric field, the built-in piezoelectric field inside the $\text{BiFeO}_3@ \text{TpPa-1-COF}$ heterojunction can act as a driving force for the efficient separation of charge carriers, and the results show that the $\Delta G_{\text{highest}}$ of $\text{BiFeO}_3@ \text{TpPa-1-COF}$ is reduced to 1.57 eV. Therefore, the piezoelectric effect significantly reduces the reaction barrier of OER, thereby exhibiting higher catalytic activity. Excitingly, the free energy curves of the four elementary reactions for all samples become downhill when the irradiation-induced external bias potential U is applied. In other words, the entire OER process can proceed spontaneously from an energy point of view. Meanwhile, **Figure 4e-f** illustrates the elementary step of HER and corresponding free energy change profiles with and without light-induced bias potential or polarized electric field for all catalysts, respectively. At $U=0 \text{ V}$ vs RHE, the free energy changes are 0.47, 0.31, and 0.21 eV of HER on TpPa-1-COF, BiFeO_3 and $\text{BiFeO}_3@ \text{TpPa-1-COF}$, respectively, which is significantly higher than the existence of piezoelectric effect (0.33, 0.25, and 0.14 eV, respectively). The light-induced external bias potential U provided by electrons is 0.6 eV for TpPa-1-COF, BiFeO_3 and $\text{BiFeO}_3@ \text{TpPa-1-COF}$, implying the photocatalytic HER is spontaneous when the sample is irradiated with visible light and ultrasound. Thence, the calculated Gibbs free energy of HER and OER verifies that the piezoelectric effect can effectively promote the overall water splitting of $\text{BiFeO}_3@ \text{TpPa-1-COF}$ under visible light. Furthermore, to elucidate the carbonyl oxygen sites

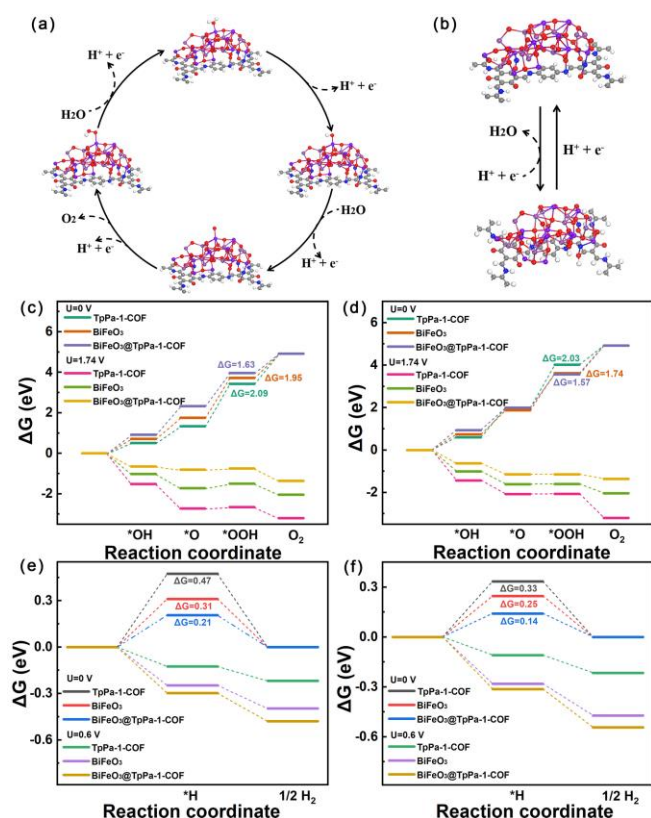


Figure 4. Proposed photocatalytic pathways of (a) OER and (b) HER with the most energetically favorable absorbed intermediates (*OH, *O, *OOH, and *H) in $\text{BiFeO}_3@ \text{TpPa-1-COF}$. The calculated Gibbs free energy changes of intermediate states involved in OER processes (c) without and (d) with piezoelectric effect, the calculated Gibbs free energy changes of intermediate states involved in HER processes (e) without and (f) with piezoelectric effect for TpPa-1-COF, BiFeO_3 and $\text{BiFeO}_3@ \text{TpPa-1-COF}$.

RESEARCH ARTICLE

in BiFeO_3 @TpPa-1-COF as the photocatalytic active center for *H coordination, another COF, COF-LZU1 without carbonyl, also binds to BiFeO_3 via covalent bonds to construct similar core-shell structured COF-LZU1@ BiFeO_3 (Figure S28-29). The typical diffraction peaks of COF-LZU1 and BiFeO_3 were observed in the PXRD pattern of COF-LZU1@ BiFeO_3 (Figure S30). As expected, the piezo-photocatalytic activity of COF-LZU1@ BiFeO_3 ($202.6 \mu\text{mol h}^{-1}\text{g}^{-1}$ of H_2 and $101.3 \mu\text{mol h}^{-1}\text{g}^{-1}$ of O_2) is much lower than that of BFO@COF20-C (Figure S31), which further reveals the HER pathway on TpPa-1-COF and BiFeO_3 @TpPa-1-COF.

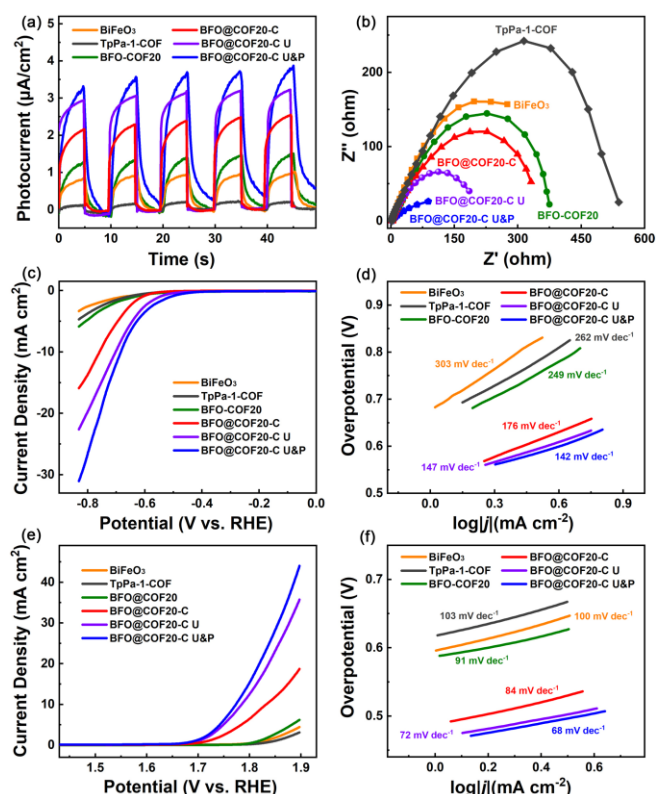


Figure 5. (a) Transient photo-current curves, (b) EIS Nyquist plots, (c) and (e) LSV curves, (d) and (f) the corresponding Tafel slopes of BiFeO_3 , TpPa-1-COF, BFO-COF20, BFO@COF20-C, BFO@COF20-C U and BFO@COF20-C U&P.

To further investigate the charge carrier transport properties of BiFeO_3 @TpPa-1-COF heterostructures, a series of photoelectrochemical measurements were conducted through a three-electrode system (Figure. S32). As presented in Figure S33, the photoluminescence (PL) intensity of BFO@COF20-C is significantly quenched compared with that of the TpPa-1-COF, BFO and BFO-COF20, indicating that the covalently bonded BFO in the heterojunction can effectively inhibit the recombination of photo-generated carriers. Simultaneously, the time-resolved photoluminescence (TRPL) spectra of samples are used to characterize the lifetime of photo-generated electron-hole pairs and the fitting results are displayed in Table S8. The lifetime of the CN20 (3.09 ns) is shorter than that of the TpPa-1-COF (3.89 ns) and BiFeO_3 (3.31 ns), which is ascribed to the more efficient electronic separation from the BiFeO_3 to TpPa-1-COF

heterostructure (Figure S34). Furthermore, the average emission lifetime of BFO@COF20-C is decreased to 1.19 ns. This confirms the existence of covalent bonds in the BFO@COF20-C heterojunction to improve the separation of photo-generated charges. As shown in Figure 5a, the results of transient photocurrent responses illustrate that BFO@COF20-C exists the highest photocurrent density compared with TpPa-1-COF, BiFeO_3 and BFO-COF20, which means easier to separate and transfer charge in BFO@COF20-C heterostructure. The electrochemical impedance spectroscopy (EIS) Nyquist plot was investigated in the dark to further clarify the charge transfer dynamics of the samples in Figure 5b. The semicircle in the Nyquist plot can be simulated well by a Randles electrical equivalent-circuit model. Obviously, the arc radius of BFO@COF20-C is smallest than that of TpPa-1-COF, BiFeO_3 and BFO-COF20. Generally, a smaller radius indicates a smaller resistance to charge transfer in the interface. In other words, the smaller the arc radius is, the faster the electron-hole pair separation and transfer is. Moreover, experimental EIS data fitted to the equivalent Randle circuit using Zview software (Table S9). As expected, the electrocatalytic HER and OER performance of BFO@COF20-C with lowest overpotential and Tafel slope (176 mA dec^{-1} of HER and 84 mA dec^{-1} of OER) further confirms the excellent separation ability of carriers (Figure 5c-f). Generally, the rapid charge transfer between piezoelectric polarization charges and electroactive species is essential to fully participate in surface charge reactions. Therefore, BFO@COF20-C was further characterized by electrochemistry under ultrasonic vibration (BFO@COF20-C U) or ultrasonic vibration and electric poling (BFO@COF20-C U&P). As shown in Figure 5a-f (the purple line), it has the higher photocurrent density, smaller resistance, overpotential and Tafel slope of BFO@COF20-C under ultrasonic vibration, while the electrochemical performance of BFO@COF20-C is further improved after polarization (the blue line in Figure 5a-f), revealing the improved charge separation and transport in the photo-piezocatalytic process by piezoelectric polarization. Contemporaneously, the piezoelectric-induced built-in electric field can tilt the CB of the BiFeO_3 nanosheets, to be slightly more negative than the $\text{H}_2/\text{H}_2\text{O}$ reduction potential (0 V) for HER (Figure 6a and S35), which also verified that the BiFeO_3 nanosheets can achieve photocatalytic hydrogen production in pure water.

The Z-scheme charge transfer process of BiFeO_3 @TpPa-1-COF was further certificated through electron paramagnetic resonance (EPR) with 5,5-dimethyl-1-pyrroline-N-oxide (DMPO) as probes. As exhibited in Figure 6b-c, only the DMPO- $\cdot\text{OH}$ signals of BiFeO_3 were observed under visible irradiation, while only the signals of DMPO- $\cdot\text{O}_2^-$ was detected for TpPa-1-COF. As expected, the EPR signals of DMPO- $\cdot\text{O}_2^-$ and DMPO- $\cdot\text{OH}$ were simultaneously detected in BiFeO_3 @TpPa-1-COF under visible irradiation, which shows higher signals than the individual BiFeO_3 and TpPa-1-COF, respectively. Moreover, no signals of DMPO- $\cdot\text{O}_2^-$ and DMPO- $\cdot\text{OH}$ were detected in the dark condition for all samples (Figure. S36), indicating that light was essential to produce reactive oxygen species. These radical spin trapping results evidence that the photocatalyst follows the Z-scheme structure rather than the conventional p-n heterojunction.

RESEARCH ARTICLE

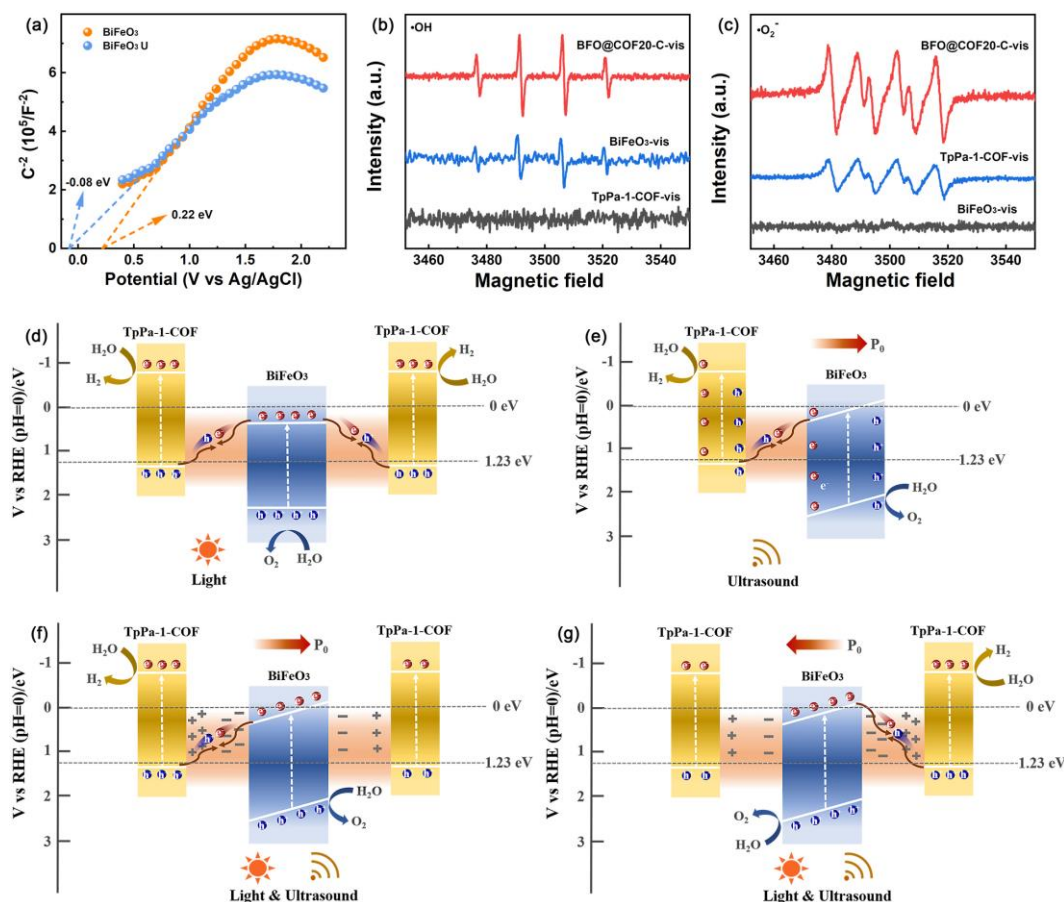


Figure 6. (a) Mott-Schottky plots for BiFeO₃ and BiFeO₃ U with 1000 Hz (under ultrasonic vibration). (b-c) DMPO spin-trapping EPR spectra of BiFeO₃, TpPa-1-COF, and BFO@COF20-C with light irradiation. Schematic diagram of (d) photocatalysis, (e) piezocatalysis and (f-g) piezo-photocatalysis with the different direction of polarization for BiFeO₃@TpPa-1-COF heterojunction.

Based on the analysis of all the above data, the possible charge transfer mechanisms for BiFeO₃@TpPa-1-COF in different overall water splitting processes are proposed. Under the excitation of sunlight, as displayed in **Figure 6d**, the photo-generated electrons in the CB of BiFeO₃ can be transferred to the VB of TpPa-1-COF to combine with the photo-generated holes. Although the photocatalytic performance is promoted to a certain extent, parts of the electron-hole pairs will recombine in the interface and/or bulk phase, inhibiting the photocatalytic reaction. When the reaction system is excited by ultrasound (**Figure 6e**), a built-in piezoelectric field (P_0) is generated inside the BiFeO₃@TpPa-1-COF heterojunction under the action of piezoelectric polarization, which drives the transfer of free electrons and holes in the opposite direction. However, some carriers will recombine at the interface between TpPa-1-COF and BiFeO₃, which greatly limits the improvement of piezoelectric catalytic performance. It is worth noting that under the combined action of light and ultrasound, the BiFeO₃@TpPa-1-COF heterojunction has the synergistic superposition advantages of the chemical potential difference and the piezoelectric potential difference. Illumination provides sufficient charge carriers assisted by ultrasonic vibrations to provide alternating built-in piezoelectric fields^[16b, 17b, 33]. Specifically, when the polarization direction of the built-in piezoelectric field is from left to right,

electrons will migrate from right to left, while holes will move in the opposite direction (**Figure 6f**). Similarly, when the polarization direction is from right to left, electrons will diffuse from left to right (**Figure 6g**). Thereby, the enhanced piezoelectric potential in the BiFeO₃@TpPa-1-COF heterojunction further accelerates the separation of electron-hole pairs, thereby enhancing the photocatalytic redox performance.

Conclusion

Summarily, we combined COF and piezoelectric material by covalent linkages and formed a series of high-efficient Z-scheme heterostructure piezo-photocatalyst for overall water splitting. The obtained BiFeO₃@TpPa-1-COF (BFO@COF20-C) photocatalyst reveals the unprecedented H₂ and O₂ production rates of 1416.4 and 708.2 $\mu\text{mol}\cdot\text{h}^{-1}\cdot\text{g}^{-1}$ under the excitations of both ultrasonication and simulated sunlight irradiation, which outperforms the reported photocatalysts and piezoelectric materials. The COF shell thickness was modulated to maximize the light utilization efficiency and the transport capacity of photo-generated carriers. Moreover, PFM revealed that the ultrasonically driven polarization potential can act as a built-in electric field to induce the separation and transfer of carriers. DFT calculations suggest that the

RESEARCH ARTICLE

piezoelectric effect promotes the reaction thermodynamic splitting of water by lowering the Gibbs free energies of HER and OER. The above advantages collectively contribute to the outstanding photo-piezocatalytic overall water splitting performance of Z-scheme BiFeO₃@TpPa-1-COF. This work has important theoretical and application value for high-efficient overall water splitting using solar and mechanical energy.

Acknowledgements

This work was financially supported by the National Natural Science Foundation of China (NSFC) (22071081, 51872121), China Postdoctoral Science Foundation (2021M692963, 2021M701270), Postdoctoral Innovation Talent Support Program (BX20220115), the Taishan Scholars Program, Case-by-Case Project for Top Outstanding Talents of Jinan, and the Opening Project of Key Laboratory of Inorganic Functional Materials and Devices, Chinese Academy of Sciences (KLIFMD202007).

Keywords: Covalent organic framework • heterostructure • piezocatalysis • photocatalysis • overall water splitting

- [1] a) Y. Ling, H. Wang, M. Liu, B. Wang, S. Li, X. Zhu, Y. Shi, H. Xia, K. Guo, Y. Hao, H. Jin, *Energy Environ. Sci.* **2022**, *15*, 1861-1871; b) S. Chen, T. Takata, K. Domen, *Nat. Rev. Mater.* **2017**, *2*, 17050; c) H. Nishiyama, T. Yamada, M. Nakabayashi, Y. Maehara, M. Yamaguchi, Y. Kuromiya, Y. Nagatsuma, H. Tokudome, S. Akiyama, T. Watanabe, R. Narushima, S. Okunaka, N. Shibata, T. Takata, T. Hisatomi, K. Domen, *Nature* **2021**, *598*, 304-307.
- [2] a) X. Chen, J. Wang, Y. Chai, Z. Zhang, Y. Zhu, *Adv. Mater.* **2021**, *33*, 2007479; b) Fujishima, Honda, *Nature* **1972**, *238*, 37-38.
- [3] a) A. Meng, L. Zhang, B. Cheng, J. Yu, *Adv. Mater.* **2019**, *31*, 1807660; b) Q. Wang, K. Domen, *Chem. Rev.* **2020**, *120*, 919-985; c) K. Li, M. Han, R. Chen, S.-L. Li, S.-L. Xie, C. Mao, X. Bu, X.-L. Cao, L.-Z. Dong, P. Feng, Y.-Q. Lan, *Adv. Mater.* **2016**, *28*, 8906-8911.
- [4] a) Q. Wang, M. Nakabayashi, T. Hisatomi, S. Sun, S. Akiyama, Z. Wang, Z. Pan, X. Xiao, T. Watanabe, T. Yamada, N. Shibata, T. Takata, K. Domen, *Nature Mater.* **2019**, *18*, 827-832; b) B. Ma, Y. Dang, D. Li, X. Wang, K. Lin, W. Wang, X. Zhou, Y. Chen, T. Xie, X. Zhang, H. Han, *Appl. Catal. B: Environ.* **2021**, *298*, 120491; c) D. Dai, X. Liang, B. Zhang, Y. Wang, Q. Wu, X. Bao, Z. Wang, Z. Zheng, H. Cheng, Y. Dai, B. Huang, P. Wang, *Adv. Sci.* **2022**, *2105299*.
- [5] D. Dai, P. Wang, X. Bao, Y. Xu, Z. Wang, Y. Guo, Z. Wang, Z. Zheng, Y. Liu, H. Cheng, B. Huang, *Chem. Eng. J.* **2022**, *433*, 134476.
- [6] a) H. Wang, Y. Yang, X. Yuan, W. Liang Teo, Y. Wu, L. Tang, Y. Zhao, *Mater. Today* **2022**, *53*, 106-133; b) S. D. Diwakara, W. S. Y. Ong, Y. H. Wijesundara, R. L. Gearhart, F. C. Herbert, S. G. Fisher, G. T. McCandless, S. B. Alahakoon, J. J. Gassensmith, S. C. Dodani, R. A. Smaldone, *J. Am. Chem. Soc.* **2022**, *144*, 2468-2473.
- [7] a) Y. Wan, L. Wang, H. Xu, X. Wu, J. Yang, *J. Am. Chem. Soc.* **2020**, *142*, 4508-4516; b) Y. Li, M. Karimi, Y.-N. Gong, N. Dai, V. Safarifar, H.-L. Jiang, *Matter* **2021**, *4*, 2230-2265; c) Y. Fu, Y. Wu, S. Chen, W. Zhang, Y. Zhang, T. Yan, B. Yang, H. Ma, *ACS Nano* **2021**, *15*, 19743-19755.
- [8] a) H. Ma, M. Wei, F. Jin, T. Chen, Y. Ma, *J. Phys. Chem. C* **2019**, *123*, 24626-24633; b) C.-F. Fu, C. Zhao, Q. Zheng, X. Li, J. Zhao, J. Yang, *China Chem.* **2020**, *63*, 1134-1141.
- [9] a) P. Dong, Y. Wang, A. Zhang, T. Cheng, X. Xi, J. Zhang, *ACS Catal.* **2021**, *11*, 13266-13279; b) C.-C. Li, M.-Y. Gao, X.-J. Sun, H.-L. Tang, H. Dong, F.-M. Zhang, *Appl. Catal. B: Environ.* **2020**, *266*, 118586.
- [10] M.-Y. Gao, C.-C. Li, H.-L. Tang, X.-J. Sun, H. Dong, F.-M. Zhang, *J. Mater. Chem. A* **2019**, *7*, 20193-20200.
- [11] Y.-P. Zhang, H.-L. Tang, H. Dong, M.-Y. Gao, C.-C. Li, X.-J. Sun, J.-Z. Wei, Y. Qu, Z.-J. Li, F.-M. Zhang, *J. Mater. Chem. A* **2020**, *8*, 4334-4340.
- [12] C. Li, G. Yu, *Small* **2021**, *17*, 2100918.
- [13] a) M. K. Mohanta, A. De Sarkar, *Nanoscale* **2020**, *12*, 22645-22657; b) P. C. Sherrell, M. Fronzi, N. A. Shepelin, A. Corletto, D. A. Winkler, M. Ford, J. G. Shapter, A. V. Ellis, *Chem. Soc. Rev.* **2022**, *51*, 650-671.
- [14] a) C. Zhang, D. Lei, C. Xie, X. Hang, C. He, H.-L. Jiang, *Adv. Mater.* **2021**, *33*, 2106308; b) Z. Jiang, X. Tan, Y. Huang, *Sci. Total Environ.* **2022**, *806*, 150924; c) S. Tu, Y. Guo, Y. Zhang, C. Hu, T. Zhang, T. Ma, H. Huang, *Adv. Funct. Mater.* **2020**, *30*, 2005158.
- [15] K. Wang, Z. Fang, X. Huang, W. Feng, Y. Wang, B. Wang, P. Liu, *Chem. Commun.* **2017**, *53*, 9765-9768.
- [16] a) H. You, Z. Wu, L. Zhang, Y. Ying, Y. Liu, L. Fei, X. Chen, Y. Jia, Y. Wang, F. Wang, S. Ju, J. Qiao, C.-H. Lam, H. Huang, *Angew. Chem. Int. Ed.* **2019**, *58*, 11779-11784; b) Y.-L. Liu, J. M. Wu, *Nano Energy* **2019**, *56*, 74-81.
- [17] a) X. Zhou, F. Yan, S. Wu, B. Shen, H. Zeng, J. Zhai, *Small* **2020**, *16*, 2001573; b) S. L. Guo, S. N. Lai, J. M. Wu, *ACS Nano* **2021**, *15*, 16106-16117.
- [18] S. Jia, Y. Su, B. Zhang, Z. Zhao, S. Li, Y. Zhang, P. Li, M. Xu, R. Ren, *Nanoscale* **2019**, *11*, 7690-7700.
- [19] Y. Feng, L. Ling, Y. Wang, Z. Xu, F. Cao, H. Li, Z. Bian, *Nano Energy* **2017**, *40*, 481-486.
- [20] Y. J. Chung, C. S. Yang, J. T. Lee, G. H. Wu, J. M. Wu, *Adv. Energy Mater.* **2020**, *10*, 2002082.
- [21] H. Li, Y. Sang, S. Chang, X. Huang, Y. Zhang, R. Yang, H. Jiang, H. Liu, Z. L. Wang, *Nano Lett.* **2015**, *15*, 2372-2379.
- [22] X. Zhou, S. Wu, C. Li, F. Yan, H. Bai, B. Shen, H. Zeng, J. Zhai, *Nano Energy* **2019**, *66*, 104127.
- [23] H. You, Z. Wu, L. Zhang, Y. Ying, Y. Liu, L. Fei, X. Chen, Y. Jia, Y. Wang, F. Wang, S. Ju, J. Qiao, C. H. Lam, H. Huang, *Angew. Chem. Int. Ed.* **2019**, *58*, 11779-11784.
- [24] J. Yin, G. Liao, J. Zhou, C. Huang, Y. Ling, P. Lu, L. Li, *Sep. Purif. Technol.* **2016**, *168*, 134-140.
- [25] S. Hong, K. L. Shuford, S. Park, *Chem. Mater.* **2011**, *23*, 2011-2013.
- [26] A. Razmjou, J. Mansouri, V. Chen, *J. Membr. Sci.* **2011**, *378*, 73-84.
- [27] Y. Wang, X. Wen, Y. Jia, M. Huang, F. Wang, X. Zhang, Y. Bai, G. Yuan, Y. Wang, *Nat. Commun.* **2020**, *11*, 1328.
- [28] a) R. Su, H. A. Hsain, M. Wu, D. Zhang, X. Hu, Z. Wang, X. Wang, F.-t. Li, X. Chen, L. Zhu, Y. Yang, Y. Yang, X. Lou, S. J. Pennycook, *Angew. Chem. Int. Ed.* **2019**, *58*, 15076-15081; b) W. Feng, J. Yuan, L. Zhang, W. Hu, Z. Wu, X. Wang, X. Huang, P. Liu, S. Zhang, *Appl. Catal. B: Environ.* **2020**, *277*, 119250; c) R. Su, Z. Wang, L. Zhu, Y. Pan, D. Zhang, H. Wen, Z.-D. Luo, L. Li, F.-t. Li, M. Wu, L. He, P. Sharma, J. Seidel, *Angew. Chem. Int. Ed.* **2021**, *60*, 16019-16026.
- [29] a) L. Wang, Y. Wan, Y. Ding, S. Wu, Y. Zhang, X. Zhang, G. Zhang, Y. Xiong, X. Wu, J. Yang, H. Xu, *Adv. Mater.* **2017**, *1702428*; b) F. Guo, W. Shi, C. Zhu, H. Li, Z. Kang, *Appl. Catal. B: Environ.* **2018**, *226*, 412-420; c) D. Qu, J. Liu, X. Miao, M. Han, H. Zhang, Z. Cui, S. Sun, Z. Kang, H. Fan, Z. Sun, *Appl. Catal. B: Environ.* **2018**, *227*, 418-424; d) F. Xue, Y. Si, M. Wang, M. Liu, L. Guo, *Nano Energy* **2019**, *62*, 823-831; e) C. Wang, H. Zhang, W. Luo, T. Sun, Y. Xu, *Angew. Chem. Int. Ed.* **2021**, *60*, 25381-25390; f) S. Zhang, G. Cheng, L. Guo, N. Wang, B. Tan, S. Jin, *Angew. Chem. Int. Ed.* **2020**, *59*, 6007-6014; g) D. Kong, J. Xie, Z. Guo, D. Yang, J. Tang, *ChemCatChem* **2020**, *12*, 2708-2712; h) L. Lin, C. Wang, W. Ren, H. Ou, Y. Zhang, X. Wang, *Chem. Sci.* **2017**, *8*, 5506-5511; i) D. Zheng, X. N. Cao, X. Wang, *Angew. Chem. Int. Ed.* **2016**, *55*, 11512-11516; j) Z. Pan, Y. Zheng, F. Guo, P. Niu, X. Wang, *ChemSusChem* **2017**, *10*, 87-90; k) X. She, J. Wu, H. Xu, J. Zhong, Y. Wang, Y. Song, K. Nie, Y. Liu, Y. Yang, M.-T. F. Rodrigues, R. Vajtai, J. Lou, D. Du, H. Li, P. M. Ajayan, *Adv. Energy Mater.* **2017**, *7*, 1700025; l) W. Che, W. Cheng, T. Yao, F. Tang, W. Liu, H. Su, Y. Huang, Q. Liu, J. Liu, F. Hu, Z. Pan, Z. Sun, S. Wei, *J. Am. Chem. Soc.* **2017**, *139*, 3021-3026; m) T. Song, P. Zhang, T. Wang, A. Ali, H. Zeng, *Appl. Catal. B: Environ.* **2018**, *224*, 877-885; n) X. Chen, R. Shi, Q. Chen, Z. Zhang, W. Jiang, Y. Zhu, T. Zhang, *Nano Energy* **2019**, *59*, 644-650; o) Y. Xiong, Y. Chen, N. Yang, C. Jin, Q. Sun, *Solar RRL* **2019**, *3*, 1800341.
- [30] a) M. K. Mohanta, A. Rawat, Dimple, N. Jena, R. Ahammed, A. De Sarkar, *Nanoscale* **2019**, *11*, 21880-21890; b) S. Yuan, W. F. lo, J. Mao, Y. Chen, X. Luo, J. Hao, *ACS Appl. Nano Mater.* **2020**, *3*, 11979-11986.
- [31] A. B. Puthirath, X. Zhang, A. Krishnamoorthy, R. Xu, F. S. Samghabadi, D. C. Moore, J. Lai, T. Zhang, D. E. Sanchez, F. Zhang, N. R. Glavin, D. Litvinov, R. Vajtai, V. Swaminathan, M. Terrones, H. Zhu, P. Vashishta, P. M. Ajayan, *Adv. Mater.* **2022**, *2206425*.
- [32] G. Yasin, S. Ibraheem, S. Ali, M. Arif, S. Ibrahim, R. Iqbal, A. Kumar, M. Tabish, M. A. Mushtaq, A. Saad, H. Xu, W. Zhao, *Mater. Today* **2022**, *23*, 100634.
- [33] M. K. Mohanta, A. Rawat, N. Jena, Dimple, R. Ahammed, A. De Sarkar, *ACS Appl. Mater. Interfaces* **2020**, *12*, 3114-3126.

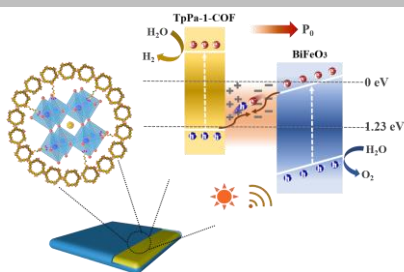
RESEARCH ARTICLE

Table of Contents

RESEARCH ARTICLE

Text for Table of Contents

We combined covalent organic frameworks (COFs) and piezoelectric material by covalent bonds to form a high-efficient Z-scheme core@shell heterostructure piezo-photocatalyst with tunable shell thickness for overall water splitting. The optimal sample reveals the unprecedented H_2 and O_2 production rates of 1416.4 and 708.2 $\mu\text{mol}\cdot\text{h}^{-1}\cdot\text{g}^{-1}$ under the excitation of ultrasonication coupled with visible light irradiation. This work will provide a new sight for the practical application of highly efficient photocatalytic overall water splitting.



Mei-Ling Xu, Meng Lu, Guan-Ying Qin,
Xiu-Mei Wu, Ting Yu, Li-Na Zhang, Kui
Li, *Xin Cheng, * Ya-Qian Lanc*

Page No. – Page No.

**Piezo-Photocatalytic Synergy in
BiFeO₃@COF Z-Scheme
Heterostructure for High-
Efficiency Overall Water Splitting**

Accepted Manuscript